Journal of Manufacturing Processes 68 (2021) 1176–1190

Contents lists available at ScienceDirect

Journal of Manufacturing Processes

journal homepage: www.elsevier.com/locate/manpro

Technical paper

Friction welding of dissimilar joints copper-stainless steel pipe consist of 0.06 wall thickness to pipe diameter ratio

Hardik D. Vyas [a], Kush P. Mehta [a,b,*], Vishvesh Badheka [a], Bharat Doshi [c]

[a] Department of Mechanical Engineering, School of Technology, Pandit Deendayal Energy University (Formerly Pandit Deendayal Petroleum University (PDPU)), Raisan, Gandhinagar, Gujarat, India
[b] LUT Mechanical Engineering, School of Energy Systems, LUT University, Yliopistonkatu 34, Lappeenranta 53850, Finland
[c] Institute for Plasma Research, Gandhinagar, Gujarat, India

ARTICLE INFO

Keywords:
Copper
Friction welding
Joint characterization
Joint properties
Pipe joints
Stainless steel

ABSTRACT

This paper examines dissimilar friction welding between electrolytic tough pitch copper (ETP-Cu) and stainless steel (SS) of grade 304 L for pipe joint configuration, having 0.06 wall thickness to pipe diameter ratio. The welding is performed using the continuous drive friction welding method. The welded joint is evaluated by visual inspection, leak-proof ability by helium leak detection testing, microstructure features by optical and scanning electron microscopy, energy dispersive x-ray spectroscope, x-ray diffraction patterns, tensile testing, and hardness measurements. The continuity of welding is evaluated by peripheral inspection and testing on four different locations of pipe welded joint. The results revealed that sound joints between dissimilar materials of Cu-SS are established with evidence of resistance to leak at room temperature and after cryogenic shock test. The Cu-SS pipe joint received excellent strength of 242.48 N/mm^2, which is nearly 80% of ETP-Cu base material. The microstructure changes are distinctly observed at the Cu side, whereas no significant microstructure changes are observed at the SS side. The microstructure features are consisting of full dynamic recrystallization zone and partial dynamic recrystallization zone that are identified at the Cu side. However, no adverse effect of microstructure on tensile strength and hardness is observed. The weld continuity in the periphery of pipe configuration is observed at four different locations. A continuous reaction layer at four investigated locations is identified, with the presence of Cu and Fe elements at the joint interface.

1. Introduction

Dissimilar materials welding is an extraordinary solution that leads to a number of benefits in terms of making lightweight structures, a combination of different properties within a single component, economic benefit by overall cost reduction, and efficiency enhancement by novel engineering solutions [1–8]. Copper (Cu) and stainless steel (SS) is one of such dissimilar materials combinations having dissimilarities in physical, chemical, and thermal properties [9–13]. However, welding of Cu-SS is an important area of interest due to the benefits of having different thermal properties at both ends, cost savings and enhancement of thermal and mechanical efficiencies of heat exchangers, and many interesting engineering applications. Despite of interesting engineering solutions and subsequent applications, welding of Cu-SS combination is challenging due to the dissimilarities in metallurgical properties. Considering the major difficulties in welding of this dissimilar combination Cu-SS joint, conventional fusion welding technologies are not suitable to obtain sound and defects free joints [14–17]. However, laser based fusion welding is observed as one of the best feasible solutions as an advanced fusion welding process for Cu-SS joints. Zhang et al. [18] performed laser welding for feasibility investigation of pure copper to SS304L materials. They used nickel based alloy as an interlayer metal between Cu to SS joint with improved joint properties. Gu et al. [19] investigated laser welding technique with continue wire feeding method on dissimilar joints between T2 copper to 301 SS base metals. They used two different filler wires such as alloy 600 and ERNiCu-7 and revealed that ERNiCu-7 wire is suitable to achieve higher tensile strength as compared to welds produced by alloy 600. Besides, the solid-state welding technologies that are operated below the melting temperature of base materials, found to be feasible for dissimilar materials welding of

* Corresponding author at: Department of Mechanical Engineering, School of Technology, Pandit Deendayal Energy University (Formerly Pandit Deendayal Petroleum University (PDPU)), Raisan, Gandhinagar, Gujarat, India.
E-mail addresses: kush.mehta@lut.fi, kush.mehta@lut.fi (K.P. Mehta).

https://doi.org/10.1016/j.jmapro.2021.06.050
Received 16 March 2021; Received in revised form 18 June 2021; Accepted 18 June 2021
Available online 29 June 2021
1526-6125/© 2021 The Author(s). Published by Elsevier Ltd on behalf of The Society of Manufacturing Engineers. This is an open access article under the CC BY license (http://creativecommons.org/licenses/by/4.0/).

Table 1
Chemical composition of the base materials.

SS 304L element	C	Mn	Si	Cr	Ni	P	S	Fe
wt%	0.028	1.14	0.36	18.36	8.2	0.026	0.002	Balance
ETP-Cu element	Cu		Pb		P		Si	
wt%	99.99		0.002		0.005		0.005	

Table 2
Mechanical and physical properties of base materials.

Base materials	Yield strength, MPa	Ultimate tensile strength, MPa	% Elongation	Melting point °C	Coefficient of thermal expansion K^{-1}	Thermal conductivity W/m*k	Specific heat J/kg*K
SS 304 L	206	517	76.56	1454	17.3×10^{-6}	16.2	500
ETP-Cu	244	306	24.16	1083	17.7×10^{-6}	390	0.386

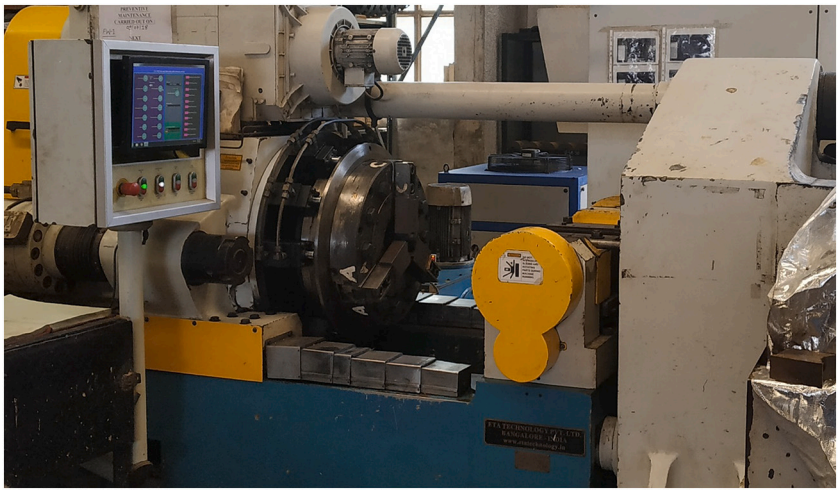

Fig. 1. Continuous drive friction welding machine.

Cu-SS joints [20–22]. Friction welding and its variants are suitable technologies to obtain defect-free Cu-SS joint, as they operate within the solid-state domain of base materials.

Jayabharath et al. [23] applied continuous drive friction welding on cylindrical rods to obtain dissimilar joints between steel (produced by powder metallurgy) and commercially pure wrought copper materials. They investigated different processing conditions by varying process parameters of friction welding and suggested a set of parametric combinations that resulted in enhanced joint properties. Kimura et al. [24] investigated dissimilar joints of oxygen-free copper to low carbon steel materials on cylindrical rods, by continuous drive friction welding. They studied joint efficiency influenced by friction time and forge pressure. Kimura et al. [25] studied friction welding on the cylindrical bar for a dissimilar combination of brass and low carbon steel joints. They investigated different welding conditions on joining phenomena and joint strength. They also found cracks at periphery towards brass material, but also received equal joint strength as compared to a brass base material. In another study by Kimura et al. [20], friction welded brass and low carbon steel joints are subjected to post-weld heat treatment that in turn decreased its joint efficiency. Ambroziak et al. [26] investigated friction welding on cylindrical rod configuration for dissimilar materials of copper to austenitic steel and copper to titanium-zirconium-molybdenum alloy joints. They observed micro-crack near the faying surface towards copper material in case of copper to austenitic steel joint. Yeoh et al. [27] applied friction welding technique on the cylindrical solid bar for dissimilar materials of copper C1100 and AISI 1030 steel joints. Wang et al. [28] studied the application of inertia radial friction welding for a dissimilar welding of copper ring to 35-CrMnSi steel rod. In another study of radial friction welding between H90 brass and D60 steel materials by Luo et al. [29], the welding is performed on a steel tube with a brass ring on it. They observed minor defects towards the welding interface in addition to diffusion evidence at other regions of the interface. Wu et al. [30] investigated inertia radial friction welding between H96 brass and 35-CrMnSi steel combination. They obtained defect-free joint and observed different microstructures influenced by thermo mechanical action during radial friction welding. Sahin et al. [31] investigated dissimilar welding between H21 steel and copper alloy of 1015 by friction welding with heat transfer mechanism. They introduced a transient two-dimensional heat transfer model to predict the variation of heat transfer along with a variation of process parameters. Luo et al. [32] studied the inertia radial friction welding for H90 brass-D60 steel joints. The authors claimed that, after welding, in the thermo mechanical affected zone (TMAZ), microstructure consisting of bainite and martensite is developed, and due to that the microhardness is increased at the faying zone. Vairamani et al. [33] examined friction welding in case of SS 304 to Cu alloy. They optimized parameters using response surface method and ANOVA. Ochi et al. [34] investigated copper alloy to steel by friction welding, and reported weld joint efficiencies in the range of 61% to 77%. Marimuthu et al. [35] applied rotary friction welding for solid bar of dissimilar materials of Monel to ETP-Cu joints and improved the strength as 231 MPa using high pressure in combination with processing parameters of friction welding.

From the available literature, it is found that the majority of the articles are investigated on cylindrical rod configuration or radial lap joint configuration having a tube of steel and O-ring of Cu. There is no

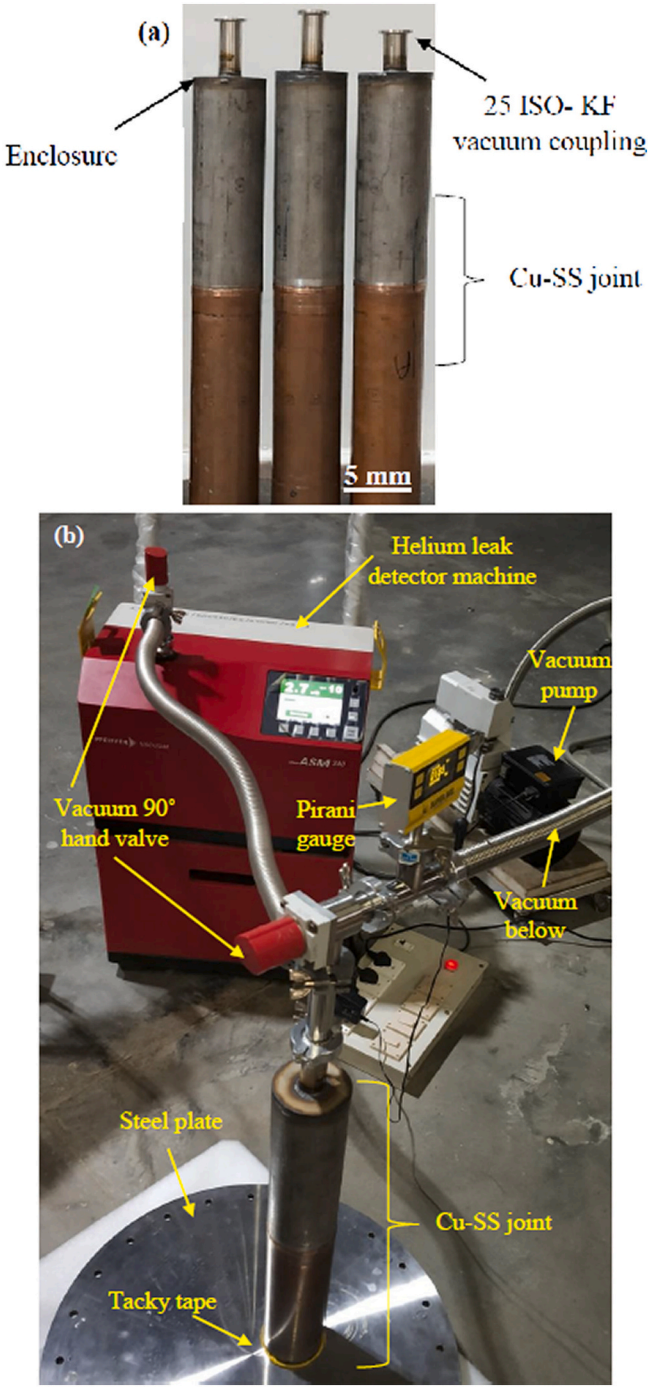

Fig. 2. (a) Welded specimens prepared for helium leak detection test, and (b) arrangement of mass spectrometer leak detector for helium leak detection.

article available that shows studies on pipe joint configuration for Cu and steel friction welding. Therefore, in the present investigation, dissimilar Cu-SS friction welding is studied on pipe joint configuration consisting of wall thickness to pipe diameter ratio as 0.060 (with a pipe diameter of 88.90 mm and a wall thickness of 5.4 mm), which is different than studies observed so far. The processing conditions are varied using different rotational speeds from the friction welding machine. The welded samples are tested for a helium leak test, cryogenic shock test, tensile testing, and microstructure characterization to evaluate the applicability of Cu-SS pipe joints in a cryogenic heat exchanger, which is performed for the first time to the best of the authors' knowledge.

2. Materials and methods

In the present investigation, the pipes of base materials such as electrolyte tough pitch copper (ETP-Cu) and SS alloy of 304 L are friction welded. Tables 1 and 2 present the chemical composition, and mechanical & physical properties of base materials respectively. The matching pipe dimensions such as outer diameter of 88.90 mm and wall thickness of 5.4 mm are prepared using machining for both Cu and SS materials. The surfaces to be subjected for welding are cleaned by acetone after machining.

During experiments of friction welding, the pipe of SS material is fixed on a three-jaw chuck that rotates during operation, while the pipe of Cu is fixed on other ends that do not rotates but hold the workpiece rigidly from the circumference clamping. The welding experiments are performed on a dedicated continuous drive friction welding machine of ETA technologies, 150 T model, as shown in Fig. 1. Before the selection of process parameters for the present investigation, feasibility trials are performed based on hands-on experience and previously published studies [36,37]. The processing conditions are varied using the set value of different rotational speeds in a friction welding machine. The input values of rotational speeds are set to 250 rpm, 300 rpm, 350 rpm, and 400 rpm, in order to investigate four different processing conditions. Other process parameters are friction time of 15 s, friction force of 8.2 t, an upset force of 16.4 t and upset time of 5 s, which are kept constant during experiments. After the welding, the welded samples are subjected to testing and characterization in order to evaluate the joint properties and microstructures. Visual inspection, helium leak test, cryogenic shock test, tensile test with fracture surface inspection by scanning electron microscopy (SEM), microstructure observations using optical microscopy and SEM, electron dispersive x-ray spectroscopy (EDS) on a joint interface, x-ray diffraction (XRD) plots and micro-hardness measurements are performed on welded samples. After the visual inspection, the flash is removed by turning and boring operations for subsequent testing and characterizations.

The welded samples are subjected to a helium leak test. Fig. 2 (a) shows arrangements for the preparation of samples for a helium leak test, wherein Cu end and SS end are closed using enclosures while SS enclosure is mounted with 25 ISO-KF (Klein Flange) coupling. SS side is closed using gas tungsten arc welding whereas the Cu side is closed using vacuum tacky tape. Setup for helium leak test with mass spectrometer leak detector (MSLD) is shown in Fig. 2 (b). In MSLD test, Pfeiffer make of ASM 340 helium leak detector is used. Before subjecting samples to MSLD, the pressure within the pipe join sample is created (in the range of 10^{-2} to 10^{-3} millibar (m bar), as background reading) using a vacuum pump. After which, the sample is transferred to the MSLD as shown in Fig. 2 (b). With the help of the MSLD machine, the vacuum leak rate is increased in the range of ultra-high vacuum (UHV) testing such as 10^{-9} to 10^{-12} m bar l/s (that is noted as initial leak rate reading). After that, the highly pressurized helium gas is sprayed on the joint area from the outer surface, with a fixed pressure of 0.14 bars (that is noted as helium spray time leak rate reading). In case of any leakage, the helium gas is sucked, and that in turn increases the leak rate. The same samples are subjected to a cryogenic shock test. The samples are dipped into the liquid nitrogen (kept at a cryogenic temperature of 77 K) for five minutes, then pulled out and kept aside in the atmospheric conditions to reach the atmospheric temperature (of 300 K). This cycle of dipping in liquid nitrogen and keeping its aside in atmospheric conditions is repeated three times, which is defined as a cryogenic shock test. After the cryogenic shock test, the samples are again subjected to a helium leak test, as performed previously.

For the tensile testing, the specimens are extracted from the welded samples according to ASME SEC IX, using wire cut electro-discharge machining. The dimensions of tensile specimens and extracted tensile specimens are shown in Fig. 3. The tensile testing is carried out using the Universal Testing Machine, Krutam Techno-FSA / M-100 model with 1 mm/min crosshead travel speed. The gripper of tensile testing

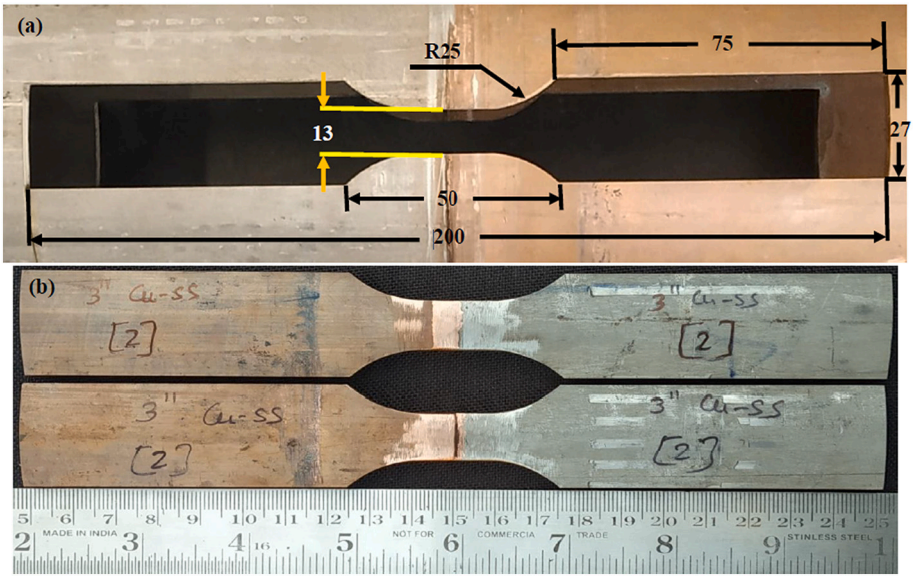

Fig. 3. Tensile specimens extracted from welds, (a) dimensions according to standards of ASME *sec* IX (all the dimensions are in mm), and (b) Extracted sample piece.

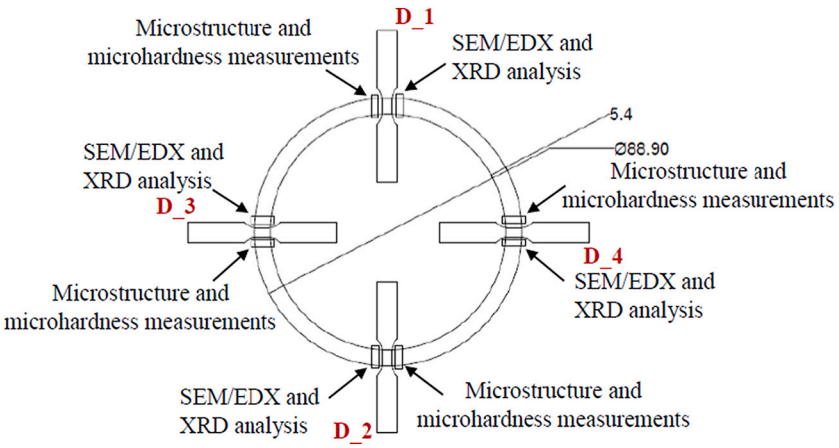

Fig. 4. Strategy image showing different locations of the specimens that are extracted for different characterizations (all dimensions are in mm).

(performed on Krutam Techno-FSA / M-100 machine) is already consisting of radian grip that is typically used for pipe joint configuration as per ASME section IX and ASTM E8 standards. The fractured surfaces of the tensile specimens are examined using SEM, ZEISS SEM 360 machine. The specimen resulted with the highest tensile strength is further subjected to microstructure analysis, x-ray diffraction analysis, and microhardness measurements. The continuity of bonding around the periphery of a circular pipe is evaluated through microstructural analysis and tensile testing at four different locations (see Fig. 4), which is considered because of distinct heat distribution and material flow that are expected around the periphery of pipe due to small thickness to diameter ratio of pipe, that may affect continuity of microstructure and mechanical properties of joint around the periphery of pipe.

The optical microstructure is performed using Olympus make microscope of BX53M model. As a part of sample preparation for optical microscopy, a standard metallographic procedure of grinding and polishing is applied, followed by etchant reagent of aqua regia (70% HNO_3 and 36% HCL) and potassium dacromet (99.99%). Further SEM and EDS analysis are performed using the FE-SEM JEOL JSM 7600F model. XRD is performed using the discover 8.0-Bruker machine. The specimen is further subjected to microhardness measurements with line mapping using the NEXUS 4302 model of the ESEWAY machine, carried out with a load of 300 g, at intervals of 100 μm from the middle of the thickness.

3. Results and discussion

3.1. Visual inspection

The visual inspection on welded samples is carried out for the flash formation and any imperfection visible through naked eyes. Fig. 5 shows weld surfaces of pipes from the outer surface and inner surface. It can be seen that the flash formation is observed as outside flash and inside flash for outer surface and inner surface respectively. There is no imperfection observed on the surfaces, whereas no major variation in flash formation is observed for all the weld conditions. Moreover, the flash formation is more from Cu material and less from SS material, due to differences in plastic deformation behaviour under applied heat and load. This flash formation subsequently helps to obtain sound weld joint as the flash removes oxides that might have formed at the time of initial rubbing action and subsequently brings new chemically active surfaces for sound metallurgical bonding. The formation of oxides can be seen on the surface of flash in terms of change of colour, in which the Cu material is contributed majorly for flash formation (that is also confirmed by microstructural analysis and presented in a subsequent section).

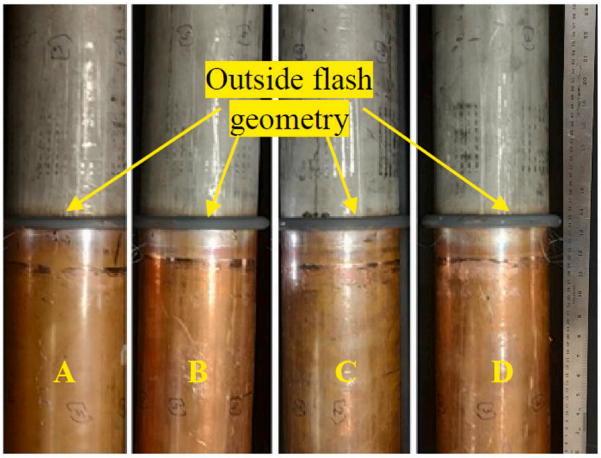

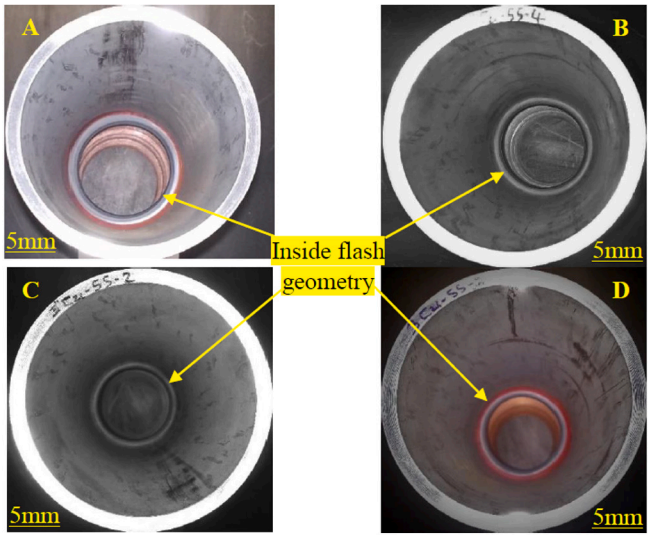

Fig. 5. The images of weld surfaces for differently applied weld conditions A, B, C, and D.

Table 3
The results for the vacuum test performed at room temperature and helium sprayed at 0.14 bar pressure.

Sample Ids / Reading	A	B	C	D
Background reading (m bar)	1.99×10^{-2}	1.98×10^{-2}	1.94×10^{-2}	2.15×10^{-2}
Initial leak rate (m bar l/s)	2.5×10^{-10}	2.6×10^{-10}	1.4×10^{-10}	1.0×10^{-9}
Helium spray time leak rate (m bar l/s)	2.6×10^{-10}	2.6×10^{-10}	1.4×10^{-10}	1.1×10^{-9}
Results	Acceptable without leak detection	Acceptable without leak detection	Acceptable without leak detection	Acceptable without leak detection

3.2. Vacuum leak detection test and cryogenics shock test

Vacuum leak tests and cryogenics shock tests are carried out to confirm the sustainability of welds in cryogenic temperature and pressurized liquid flow conditions. The results for the vacuum test performed at room temperature, using 0.14 bar of helium spray pressure, are shown in Table 3. It can be seen from background reading and leak rate reading that all the samples attained acceptance without any leak detection, which in turn confirms sound welding between Cu and SS materials. Fig. 6 shows images after the cryogenic test. It can be seen that, the specimens' undergone thermal change cycles having dipped into liquid nitrogen with cryogenic temperature of 77 K and kept aside at room temperature. The weld zone has not been influenced by possible expansion and contraction due to thermal cycles at cryogenic temperature to room temperature. The assessment of any possible defect is performed again through a vacuum leak detection test. Table 4 shows results for vacuum tests performed after cryogenic shock test and helium sprayed at 0.14 bar pressure. It can be confirmed that all the specimens have attained acceptance without any leak detection, even after the cryogenic shock test.

Fig. 6. Cryogenics shock test effect on Cu-SS joints.

Table 4
The results for the vacuum test are performed after the cryogenic shock test and helium sprayed at 0.14 bar pressure.

Sample Ids / Reading	A	B	C	D
Background reading (m bar)	1.94×10^{-2}	1.91×10^{-2}	1.98×10^{-2}	1.88×10^{-2}
Initial leak rate (m bar l/s)	3.0×10^{-10}	5.0×10^{-11}	3.5×10^{-10}	3.8×10^{-10}
Helium spray time leak rate (m bar l/s)	3.1×10^{-10}	5.4×10^{-11}	4.1×10^{-10}	4.0×10^{-10}
Results	Acceptable without leak detection	Acceptable without leak detection	Acceptable without leak detection	Acceptable without leak detection

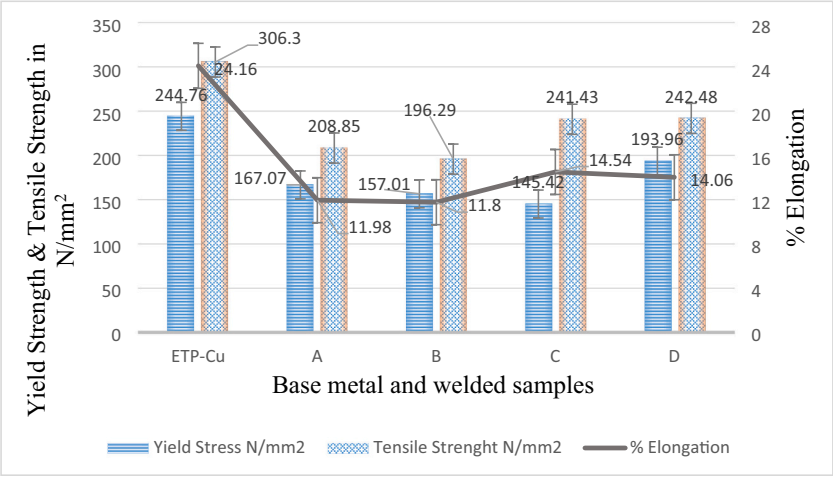

Fig. 7. Tensile testing results welded specimens under different conditions and base ETP-Cu.

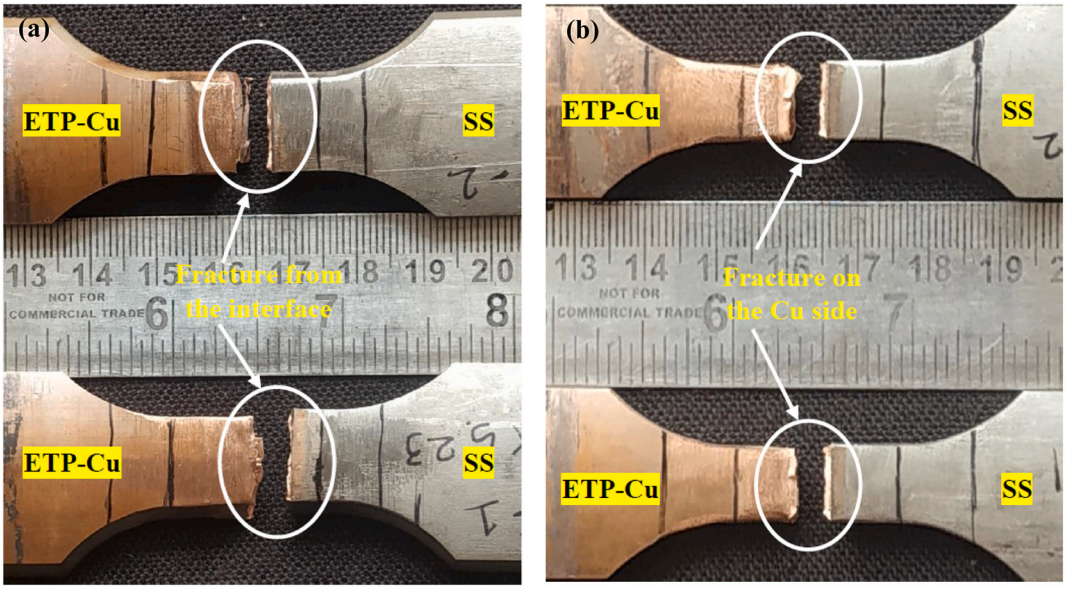

Fig. 8. Macro images of tensile specimen after tensile testing indicating fracture locations in case, (a) sample B, (b) sample D.

3.3. *Tensile test results and fracture surface inspection after tensile testing*

The tensile testing results of the welded samples are shown in Fig. 7. It can be seen that the numbers represent the average value from two specimens. The maximum ultimate tensile strength of 242.48 N/mm^2 and maximum yield strength of 193.96 N/mm^2 are observed in the case of sample D, which are nearly 80% of the Cu base material. The obtained joint efficiency in the present investigation is higher than the same observed in published articles of [9,38]. The metallurgical issues involved with dissimilar materials properties may have resulted in slightly lower tensile strength as compared to Cu base material, however that is acceptable for the application of cryogenic heat exchanger's transition joint. Out of four different welded conditions, the minimum ultimate tensile strength of 196.29 N/mm^2 and yield strength of 157.01 N/mm^2 are observed in the case of sample B. There is a small change in parametric conditions caused by only rotational speed when compared to sample D, and observing other parameters as constant. However, the welded joint of sample B has resulted as a defect-free weld with acceptable tensile strength. The elongation is observed lower as compared to Cu base material in the case of all the welded samples. In the case of sample D, the difference in elongation is 10.1% to Cu base material. This is possibly due to the formation of a reactive layer at the interface of the weld zone that may consist of hard and brittle intermetallic compounds (IMCs) and/or oxides. Further confirmation and discussion on the formation of IMCs and oxides are presented in a subsequent section. Fig. 8 shows the macroscopic images indicating fractured locations after the tensile testing in case of both the specimens such as samples B (observed with lowest ultimate tensile strength) and sample D (observed with highest tensile strength), whereas Fig. 9 shows the macroscopic top view of fractured surfaces in the case of samples B & D. It can be seen from Fig. 8(a) that the fracture location is the reaction layer (i.e. from the interface between Cu-SS joint) in case of sample B, whereas the fracture location is from the Cu side close to the Cu-SS interface (but not from the reaction layer as can be seen from Fig. 8 (b)) in case of sample D. It can be seen from Fig. 9 (a) that the fractured surfaces are mostly flat that confirms the fracture is occurred from the reaction layer in case of weld sample B, whereas peaks and valleys are observed (majorly at Cu side) on fractured surfaces of weld sample D as can be seen from Fig. 9 (b) that indicates fracture is partially from the Cu side and partially from reaction layer. However, Fig. 9 (b) also shows that large amount of Cu is available on the fracture surface towards SS side, which indicate majority of fracture from Cu side outside of reaction

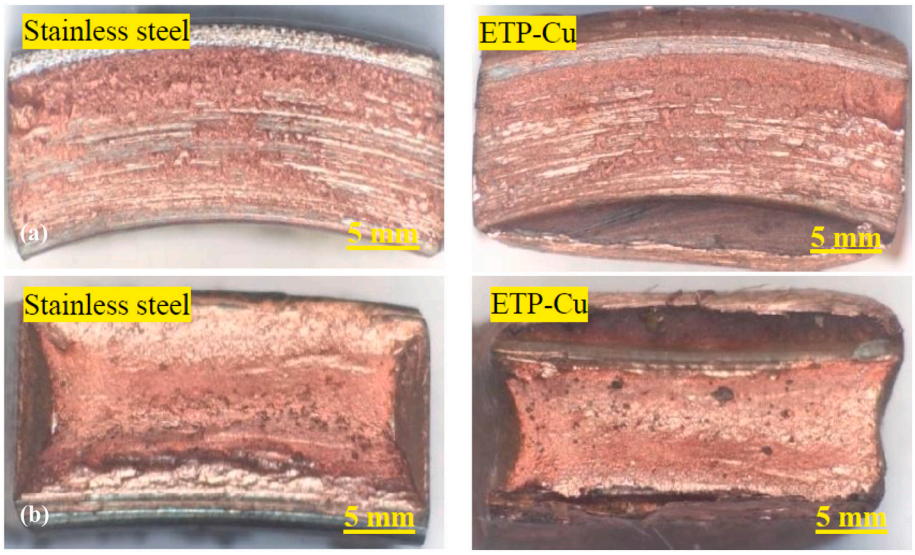

Fig. 9. Macroscopic top view of fracture surfaces after tensile testing in case of (a) sample B, and (b) sample D.

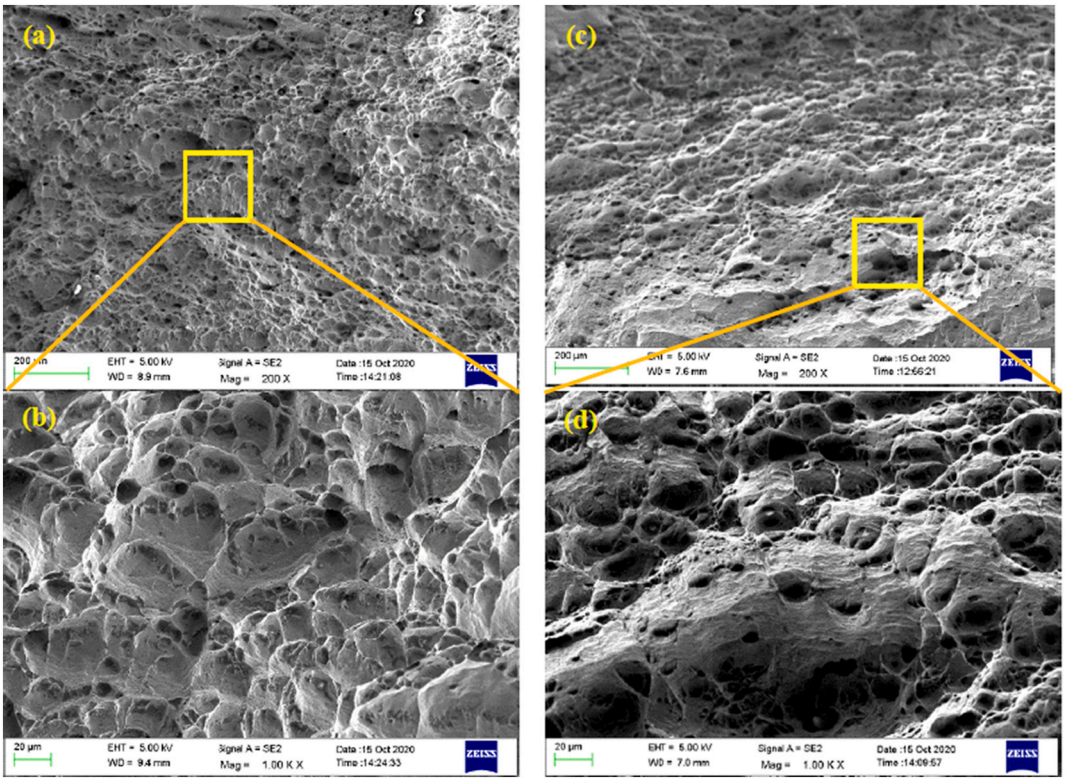

Fig. 10. SEM images of the fractured surfaces in case of sample D, (a) and (b) fractured surface images at Cu side, and (c) and (d) fractured surface images at SS side.

layer. Although, it is observed that the fracture is mainly from Cu side outside of reaction layer in case of sample D, however, the tensile strength is not equal to or higher than ETP-Cu. This is because of following two possible reasons such as (1) The fracture is not fully from Cu side, but majorly from Cu side and partially from reaction layer, which resulted in average strength between reaction layer zone and ETP-Cu; and (2) During friction welding of Cu-SS pipe configuration, the microstructure of Cu is significantly affected due to thermo mechanical processing. This in turn resulted in distinct microstructure features within small processed zones near to the interface region towards Cu. The heterogeneous microstructure at Cu side adjacent to the interface region may have affected tensile strength, and resulted fracture from that region may have caused lower tensile strength as compared to the base material of ETP-Cu.

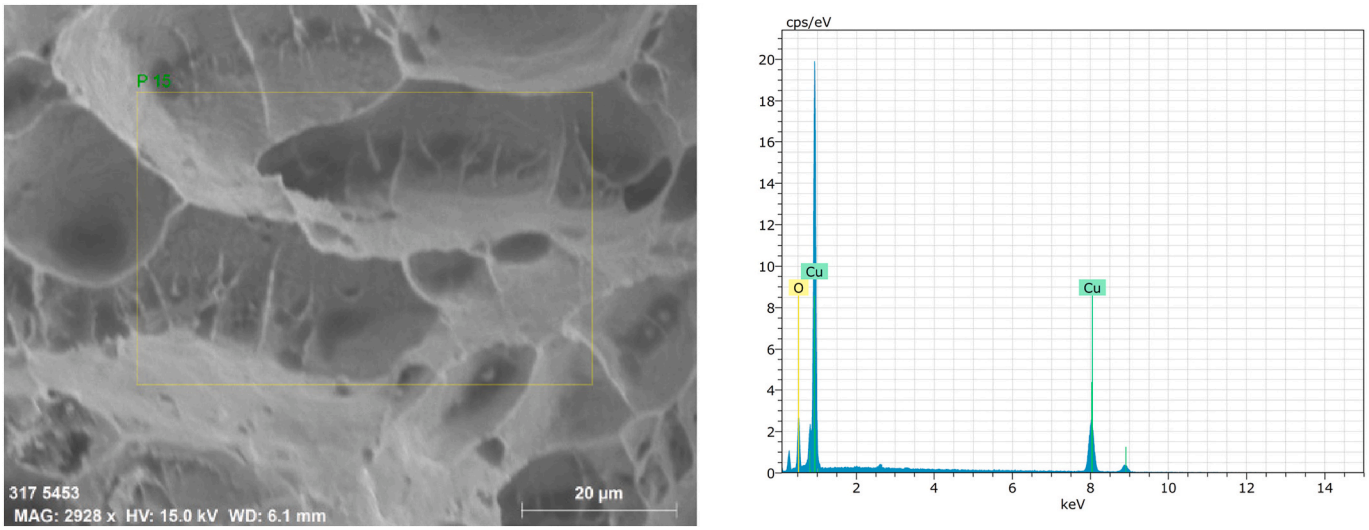

Fig. 11. EDS analysis on the fractured surface from the SS side for sample D.

In both the cases of fracture, necking is absent and surfaces are observed like a flat profile that indicates possibly of brittle fracture, which may be the reason for low elongation as observed in Fig. 7. On the other hand, SEM images shown in Fig. 10 (for weld sample D) are noticed with two different features such as micro dimples and flat surfaces. This shows a mixed fracture mode of brittle and ductile. However, a large amount of micro dimples are noticed from Fig. 10 that indicates dominant ductile fracture over brittle fracture. In Shanjeevi et al. [9], similar ductile fracture is observed for a fractured surface of tensile testing in the case of Cu-SS friction welded joints. Fig. 11 shows SEM image with EDS performed on the fractured side of SS to find the possible presence of material/elements on the fractured surface in case of sample D. It can be seen that the presence of Cu on the surface that in turn confirms the fracture is majorly from the Cu side and not only from the reaction layer of the Cu-SS joint in case of sample D.

3.4. Microstructure and characterization

The microstructure and characterization of the weld zone for sample D are presented in Fig. 12. Fig. 12 (a) shows the macrograph of the Cu-SS friction welded image of sample D. It can be seen that different locations at the interface corresponds to the macrograph in Fig. 12 (a) are noticed with different features of microstructures. The flash formation serves as a self-cleaning process to remove oxide from the faying surfaces that in turn results in a sound joint in case of the friction welding process [29]. It can be seen that from Fig. 12 (a) that the flash formation is distinguishably observed from Cu material, whereas no material participates in flash formation (based on cross-sectional image and visual observation). This is obvious because of the soft and ductile nature of Cu material as compared to SS material, under the same applied load and temperature. High magnified images of Fig. 12 (b) and (c) represent the parent metal microstructure of Cu and SS. Consequently, the material adjacent to a joint interface is majorly influenced by deformation that in turn resulted in distinct features of microstructure at the Cu side, whereas no distinct variations in microstructure at the SS side are observed. These distinct microstructures at the Cu side are identified as full dynamic recrystallization zone (FDRZ) and partial dynamic recrystallization zone (PDRZ). Similar zones are observed in [21]. FDRZ is observed at the Cu material that is very close to the interface between the Cu-SS joint (refer to Fig. 12 (g) and (i)). Within this zone of FDRZ, there are two distinct features of grains observed such as elongated grains and fine grains. The elongated grains are observed at the end surfaces from where the flash flow is noticed (refer Fig. 12 (d) and (e)), whereas the fine equi-axed grains are observed at a middle portion of a workpieces' thickness (refer Fig. 12 (g) and (i)). The elongated grains at the end surfaces of base materials are formed due to geometric dynamic recrystallization whereas fine equi-axed grains are formed may be due to discontinuous dynamic recrystallization at middle portion of workpieces' thickness. The configuration of workpiece such as small thickness of pipes may have influenced on localized strain variations at the material of interface, which in turn may leads to different grain structure within single vertical plane of cross section. The material that is near to interface experiences very high strain rate, which in turn resulted to FDRZ. There is another zone observed as PDRZ (refer Fig. 12 (d), (f) and (h)), which is adjacent to FDRZ towards Cu side, in which the material experiences low strain rate as compared to FDRZ. Therefore, this zone is termed as PDRZ, where dynamic recrystallization is experienced partially. Relative to FDRZ, larger grains are observed in PDRZ, however, they are smaller than Cu base material (Fig. 12 (b)). This PDRZ may have experienced discontinuous dynamic recrystallization. The grains with twins are also observed in PDRZ as can be seen from Fig. 12 (f) and (g), which may be due to discontinuous dynamic recrystallization. The discontinuous dynamic recrystallization is possible due to lower medium stacking fault energy of Cu base material. However, the quantitative analysis on grains and recrystallization are not carried out, considering the scope and focus of present investigation on manufacturing domain.

In addition to microstructural changes at the Cu side, a reaction layer is distinctly observed at the interface between Cu and SS joint. This reaction layer is continuous throughout the thickness of the joint. The reaction of a metallic element with oxygen may have formed oxide and existed as a reaction layer or it may be due to the formation of IMCs at the joint interface. The continuity of the reaction layer also governs joint behaviour, especially in the case of pipe joint configuration that has 0.06 wall thickness to pipe diameter ratio. Therefore, the quantitative measurements are performed to measure the reaction layer at the periphery of welded joints in the case of sample D. Fig. 13 shows images of Cu-SS interface with measurements of reaction layer in case of four different samples extracted from different locations of pipe joint periphery corresponding to Ids: D_1 to D_4 in Fig. 4. Table 5 shows the corresponding measured value of reaction layer thickness at different locations indicated in Fig. 13. It can be seen that the reaction layer is continuous and its thickness is in the range of 2 µm to 48 µm. The average thickness of the reaction layer is observed as 26.222 µm, 20.296 µm, 25.782 µm, and 12 µm for D_1, D_2, D_3, and D_4 respectively. This confirms continuous reaction and subsequent metallurgical bonding at the periphery of pipe

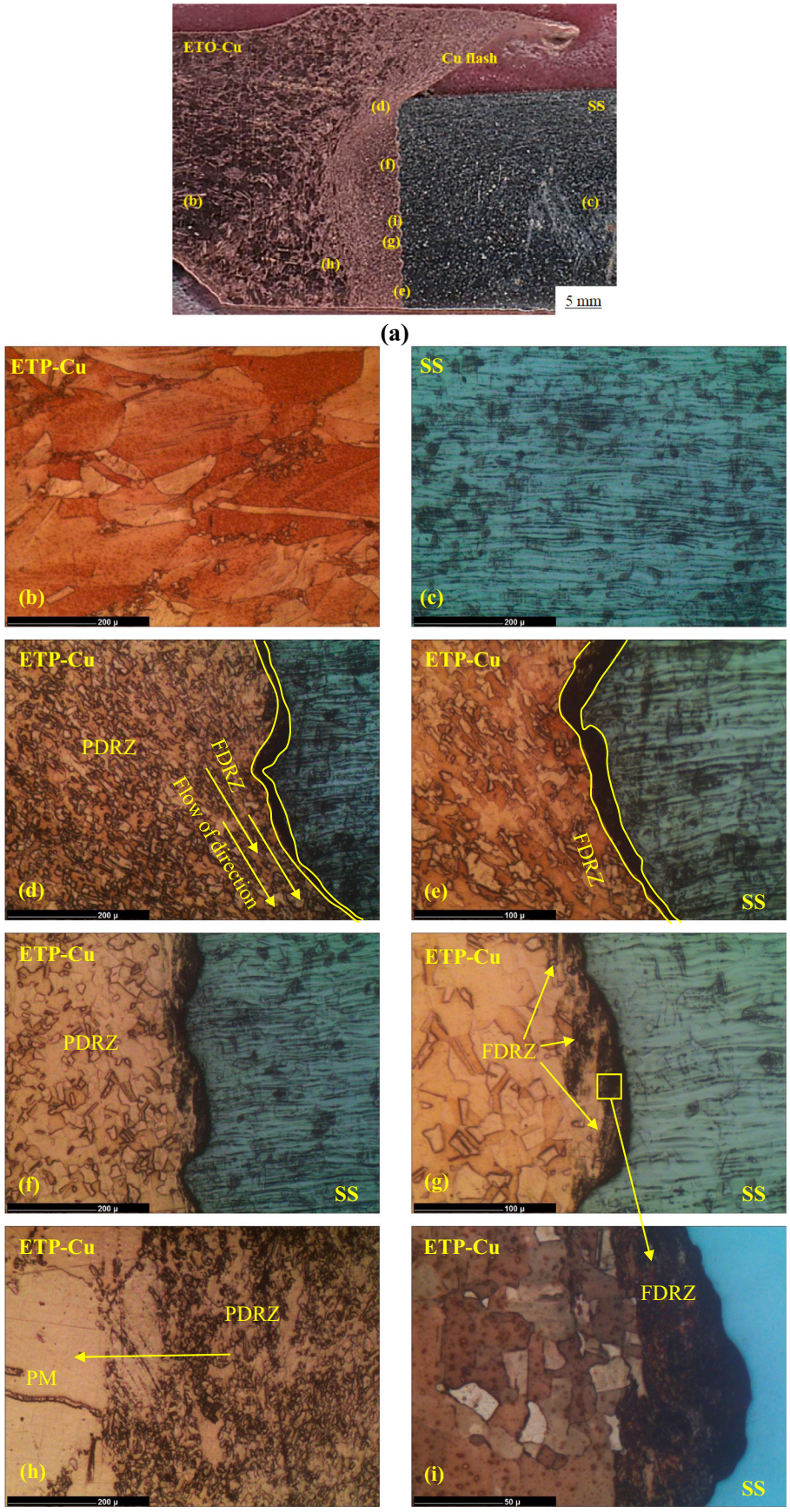

Fig. 12. Microstructure images of Cu-SS joint of Sample D, (a) Macrograph of Cu-SS interface, (b) Cu base material, (c) SS base material, (d) PDRZ, FDRZ with elongated grains in flow direction flash and Cu-SS interface, (e) Cu-SS interface at the bottom side of thickness showing elongated grains at Cu side, (f) PDRZ and Cu-SS interface at the middle of thickness, (g) FDRZ near to interface, (h) PDRZ and Cu base material interface, (i) FDRZ near the interface.

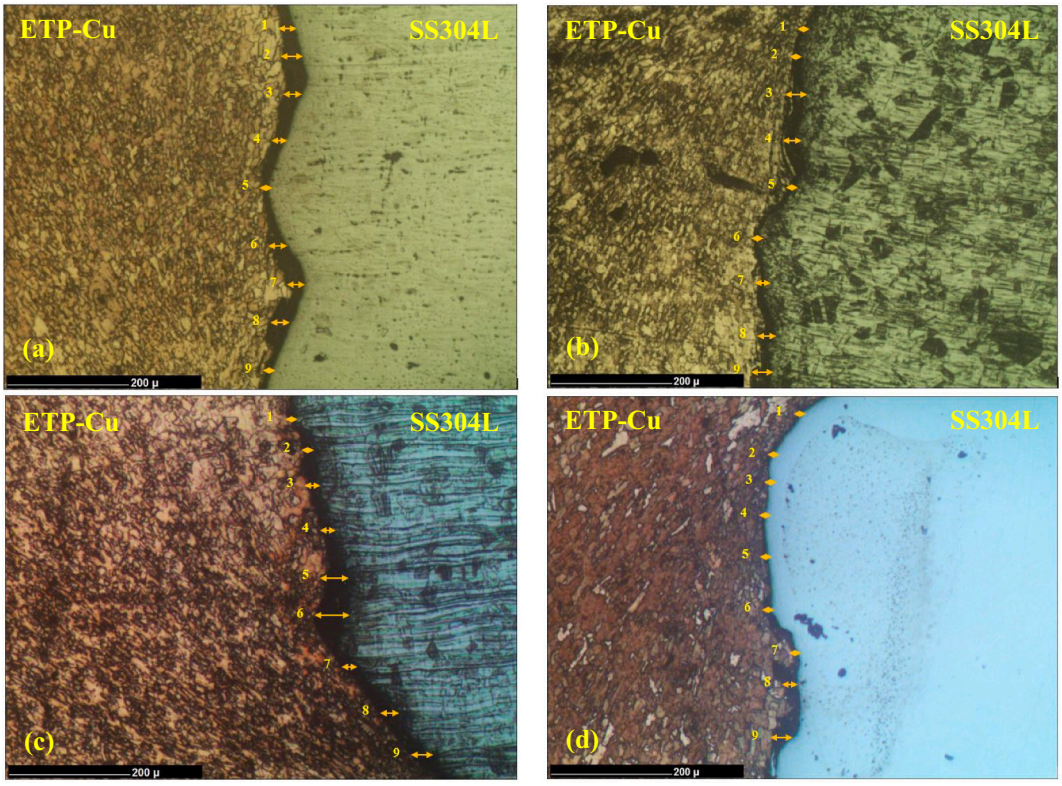

Fig. 13. Microstructure images indicating measurement location of reaction layer in case of sample D corresponding to Fig. 4: (a) D_1, (b) D_2, (c) D_3, and (d) D_4.

Table 5
Reaction layer thickness measurements at different locations of sample D's periphery.

Reaction layer thickness in a different location in µm	Location D_1	Location D_2	Location D_3	Location D_4
1	24	13.333	13.333	8
2	34.667	16	17.333	5.333
3	29.333	32	18.667	2.667
4	21.333	28	21.375	6.667
5	8	12	42.667	6.667
6	30.667	13.333	48	16
7	33.333	9.333	20	12
8	38.667	26.667	26.667	24
9	16	32	24	26.667
Average reaction layer thickness in µm	26.222	20.296	25.782	12

welded Cu-SS joints. The variation of the reaction layer's thickness is may be due to different heat distribution and material flow that is resulted under a small ratio of pipe thickness to the pipe diameter. It is noted in [39,40] that the reaction layer thickness is driven by processing temperature and reaction time. However, the variation of reaction layer thickness is not so significant for variation in mechanical properties. This is confirmed by tensile testing for samples D_1 to D_4 shown in Fig. 4. Fig. 14 shows results of ultimate tensile strength is observed without significant variation in value such as 252 N/mm^2 (D_1 location), 232 N/mm^2 (D_2 location), 232.58 N/mm^2 (D_3 location), and 233.45 N/mm^2 (D_4 location) in case of sample D.

3.5. Cu-SS joint interface with scanning electron microscopy (SEM) and energy dispersive X-ray spectrograph (EDS)

The interface between Cu-SS is investigated by SEM and EDS. A thin reaction layer is distinctly observed, as can be seen from Fig. 15. Images in Fig. 15 (b)-(i) show elemental line mapping of Cu and iron (Fe) elements at the interface region. Different images are showing interface region corresponding to four different locations shown in Fig. 4 (D_1 to D_4). The diffusion layer can be seen from Fig. 15 (a), whereas the continuous presence of elements Cu and Fe can be seen at the interface region between Cu-SS in the case of all the images Fig. 15 (b)-(i). This confirms continuous bonding between Cu-SS throughout the periphery of pipe joint configuration. In addition to Cu and Fe elements, other elements are also presented at the line mapped area in all the images as can be seen from Table 6. Other elements such as Si, Ni, and Cr are reported as can be seen from Fig. 16. The interface region in all the images such as Fig. 15 (b)-(i) confirms reaction layer is consisting elements of Cu and Fe that is having a thickness similar that are measured and presented in Fig. 13 and Table 5. In the case of friction welding, the maximum operating temperature at the interface of a workpiece is nearly around 80% of the melting temperature, which is around 800 °C or less than that in the present investigation. Hence, the solid-state interdiffusion between Cu-SS materials is the strong possible cause for the observed reaction layer at the interface. Elemental diffusion can be detected from the chemical characterization of the interface region of the Cu-SS dissimilar joint as presented in Fig. 15 and Table 6.

Comparing the results of Fig. 14 and Table 6, it can be observed that there is a variation in weight % of Cu, Fe and other elements (Table 6). However, no significant variations in ultimate tensile strength are observed (Fig. 14). This is observed may be due to fracture location is outside of reaction layer (i.e. majorly from Cu side) as observed in Figs. 8 and 9. Therefore, variations in elements at the reaction layer have not affected the tensile strength, but affected may be due to variations in

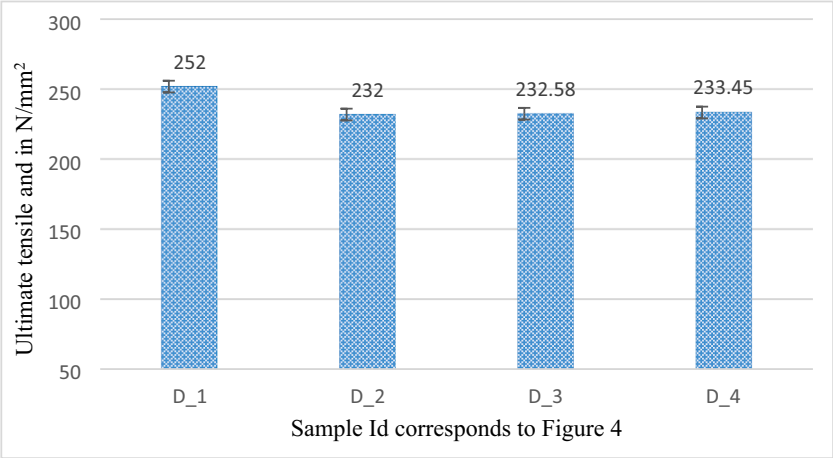

Fig. 14. Tensile strength at different locations of sample D's periphery corresponding to Fig. 4.

microstructure features that are observed with similar features as can be seen from Fig. 12.

X-ray diffraction (XRD) patterns for sample D condition are shown in Fig. 17. The phases such as Cu, Fe, $FeCu_4$, and Cu_9Si are identified in XRD, at which phases of $FeCu_4$ and Cu_9Si are IMCs. The IMCs are formed because of solid-state interdiffusion between elements of Fe & Cu and Cu & Si. These phases of IMCs are also reported in Wang et al. [28], which is investigated for dissimilar friction welding of T3 copper and 35CrMnSi steel. These phases may have caused hard and brittle structures that in turn have resulted in poor elongation during tensile testing. The reaction layer observed at the interface between the Cu-SS joint is possibly consisting of these IMCs phases of $FeCu_4$ and Cu_9Si.

3.6. Microhardness measurements

The microhardness measurements are carried out for all four samples such as D_1, D_2, D_3, and D_4 that are extracted from sample D's pipe periphery mentioned in Fig. 4. Fig. 18 shows microhardness measurements for all four samples. The hardness is observed in a large range of 50 HV to 277 HV, because of a large difference in hardness of Cu and SS material. Lower hardness is observed on the Cu side whereas higher hardness is observed on the SS side. However, there is no major difference in hardness observed for D_1, D_2, D_3, and D_4. On the Cu side, the hardness is in the range of 62.9 to 75.4 HV. In the location of the interface, the hardness increased and the value is 72.6 to 115.3 HV. The hardness in the range of 170 HV to 277 HV is observed on the SS side. In case of sample D_3, increased hardness value of 277 HV is observed at the interface region towards SS side, whereas no such increased hardness is observed in other samples of D_1, D_2 and D_4. This can be correlated from Table 6 (D_3), where Fe element is observed as 33.67% and Cu element is observed as 52.35%. It can be interpreted as higher diffusion of Fe in Cu as compared to other conditions. This higher diffusion of Fe in Cu may have formed ferrite supersaturated region with Cu [41], when subjected to heating and cooling during friction welding. This may be the reason for highest hardness at the reaction layer region in case of D_3. On the other hand, minor increased hardness at interface region in case of samples of D_1, D_2 and D_4 as compared to the hardness of Cu base material is observed that may be because of different possible reasons such as the formation of IMCs or grain refinement after severe plastic deformation or combined effect of both. In the literature of [28,42,43], fine grain refinement and solid solution strengthening by work hardening are reasoned for higher hardness at interface region in the case of Cu-SS friction welding.

4. Conclusions

In the present investigation, dissimilar friction welding on Cu-SS materials is successfully studied for pipe joint configuration, consisting of wall thickness to pipe diameter ratio as 0.060 (with a pipe diameter of 88.90 mm and a wall thickness of 5.4 mm). The following conclusion can be drawn from the present investigation.

- The defect-free and leak-proof dissimilar materials of Cu-SS pipe joints are successfully welded by friction welding, which are suitable to operate in cryogenic heat exchanger application.
- Maximum ultimate tensile strength of 242.48 N/mm^2 and maximum yield strength of 193.96 N/mm^2 are obtained, which are nearly 80% of the Cu base material. In case of maximum obtained tensile strength, the tensile specimens are majorly broken from the Cu side near to the interface of reaction layer. The fractured mode is dominated by the ductile fracture with mixed fracture of ductile and brittle modes.
- The microstructure changes are significant at the Cu side near to Cu-SS weld interface, whereas no significant microstructure changes are observed at the SS side. The microstructures at the Cu side are identified as full dynamic recrystallization zone and partial dynamic recrystallization zone.
- The weld continuity in the periphery of pipe configuration is observed with less variations of microstructure features and mechanical properties at four different locations, along with evidence of a continuous reaction layer with the presence of Cu and Fe elements at the interface. The intermetallic phases such as $FeCu_4$ and Cu_9Si are identified.

Abbreviations

ETP-Cu	Electrolytic tough pitch copper
Cu	ETP-Cu
SS	Stainless steel
FDRZ	Full dynamic recrystallization zone
PDRZ	Partial dynamic recrystallization zone
PM	Parent metal
RPM	Revaluation per minutes
SEM	Scanning electron microscopy
EDS	Electron dispersive x-ray spectroscopy
XRD	X-ray diffraction analysis
IMC	Intermetallic compound

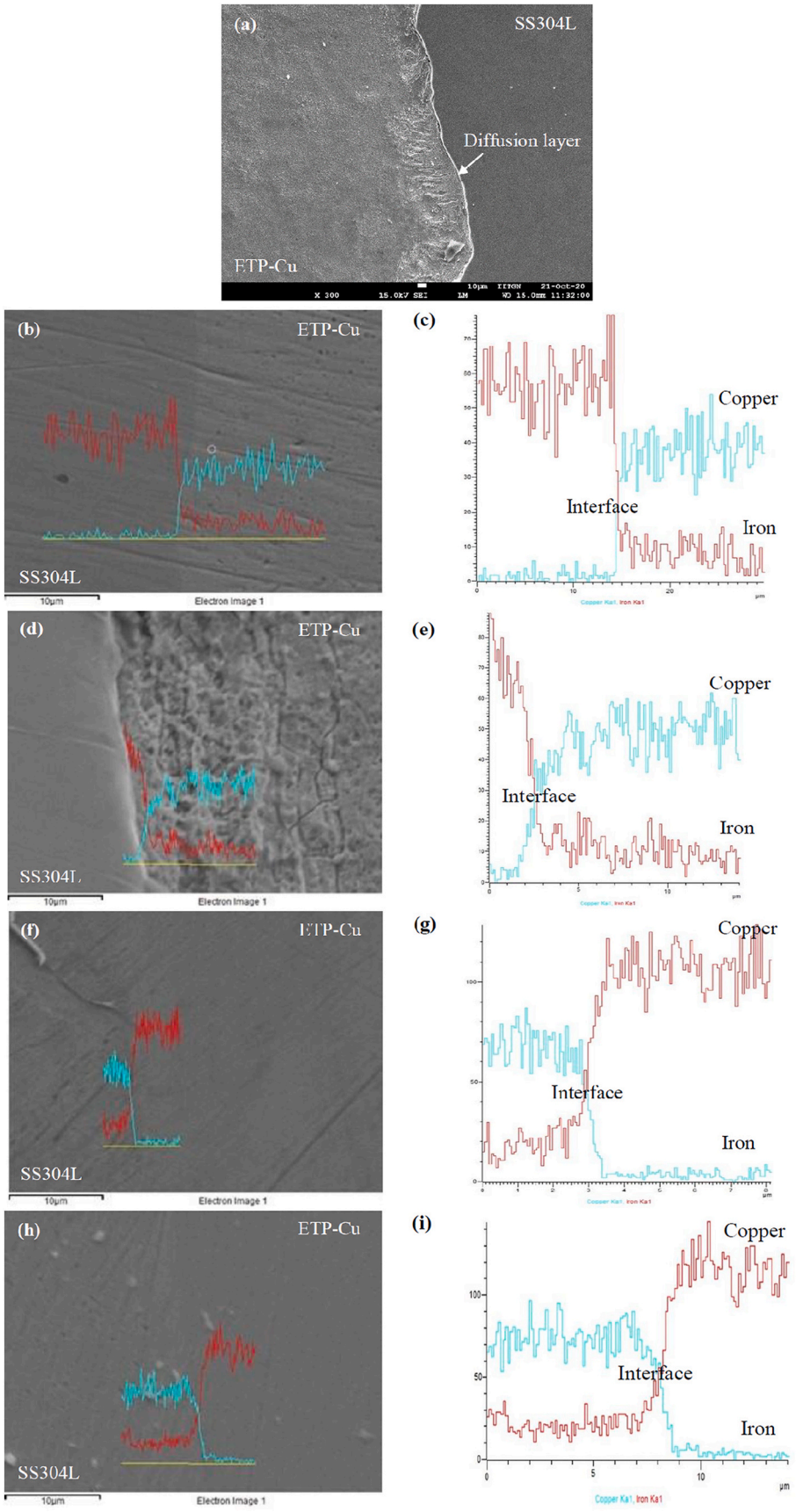

Fig. 15. SEM and EDS line scanning results of the Cu-SS interface of sample D showing interface region corresponding to peripheral locations shown in Fig. 4: (a) SEM image of an interface, (b-c) D_1, (d-e) D_2, (f-g) D_3, and (h-i) D_4.

Table 6
The weight percentage of elements at different locations of sample D's periphery.

Different location of welded sample D	Element Cu in weight%	Element Fe in weight%	Other elements in weight%
Location D_1	65.49	24.83	9.68
Location D_2	68.24	8.84	22.92
Location D_3	52.35	33.67	13.98
Location D_4	63.98	25.50	10.52

CRediT authorship contribution statement

Hardik D. Vyas: Investigation, Methodology, Resources, Experimentation, Formal analysis, Writing - original draft.

Kush P. Mehta: Conceptualization, Formal analysis, Funding acquisition, Methodology, Project administration, Resources, Supervision, Validation, Visualization, Writing - review & editing.

Vishvesh Badheka: Project administration, Resources, Technical support, Supervision.

Bharat Doshi: Supervision.

Declaration of competing interest

The authors declare that they have no known competing financial

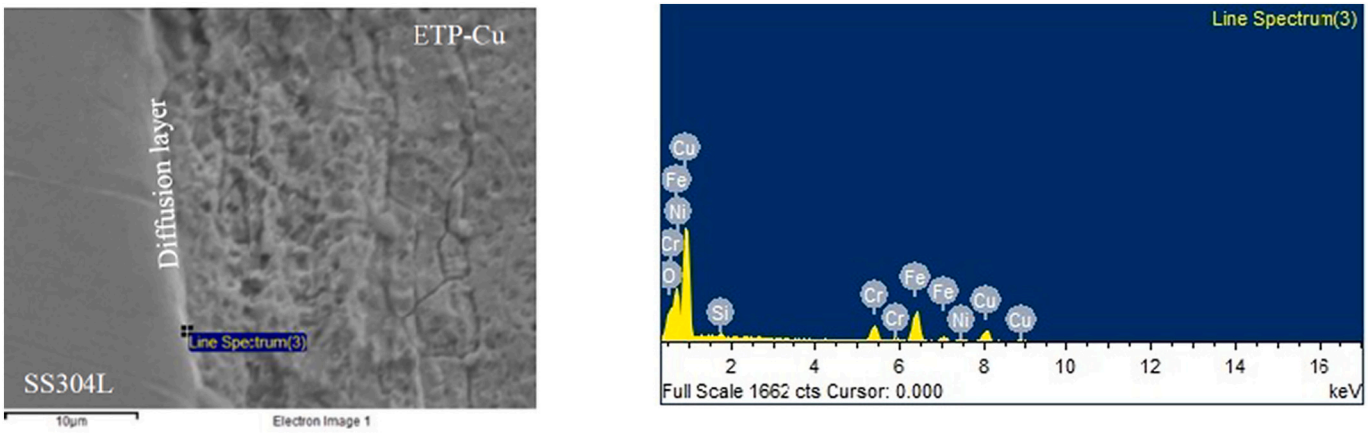

Fig. 16. SEM image with spot EDS results in the interface zone of Cu-SS joint of sample D.

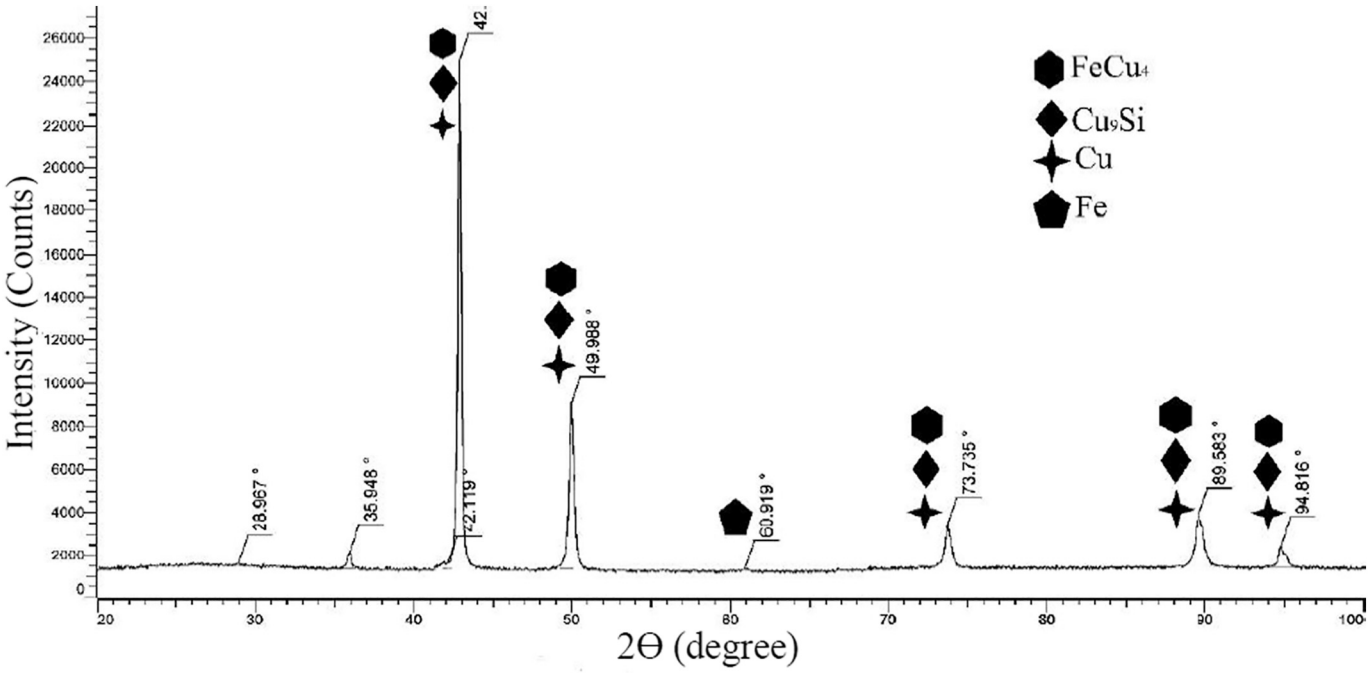

Fig. 17. XRD results for the phase identification case of sample D.

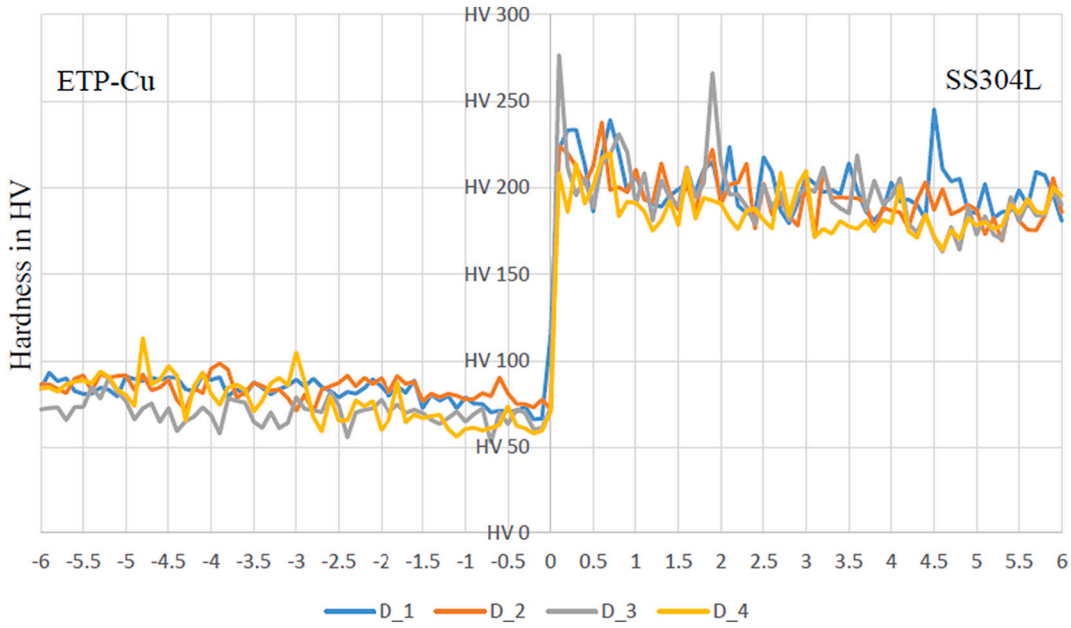

Fig. 18. Microhardness measurements for sample D, measured with 100 μm distance.

interests or personal relationships that could have appeared to influence the work reported in this paper.

Acknowledgments

This investigation is supported by a funded project of 39/14/02/2018-BRNS/39002 by the Board of Research in Nuclear Sciences (BRNS), India, which is under the developmental activity for one of the applications in Steady State Superconducting Tokamak (SST-1) of Institute for Plasma Research, Gandhinagar, India. The industry collaboration for friction welding experimental assistance from Vulcan Industrial Engineering and equipment for helium leak detection testing from Institute for Plasma Research, Gandhinagar (support extended by Mr. A. K. Sahu) are also acknowledged.

References

[1] Aritoshi M, Okita K. Friction welding of dissimilar metals. Weld Int 2003;17:271–5. https://doi.org/10.1249/01.mss.0000538518.76078.fa.
[2] Meshram SD, Mohandas T, Reddy GM. Friction welding of dissimilar pure metals. J Mater Process Technol 2007;184:330–7. https://doi.org/10.1016/j.jmatprotec.2006.11.123.
[3] Mehta KP, Badheka VJ. A review on dissimilar friction stir welding of copper to aluminum: process, properties, and variants. Mater Manuf Process 2016;31:233–54. https://doi.org/10.1080/10426914.2015.1025971.
[4] Mehta KP. A review on friction-based joining of dissimilar aluminum-steel joints. J Mater Res 2019;34:78–96. https://doi.org/10.1557/jmr.2018.332.
[5] Uzkut M, Ünlü B, Yilmaz S, Akdağ M. Friction welding and its applications in Today's world. Sarajev Int Symp Sustain Dev 2010:710–24.
[6] Uday MB, Fauzi MNA, Zuhailawati H, Ismail AB. Advances in friction welding process: a review. Sci Technol Weld Join 2010;15:534–58. https://doi.org/10.1179/136217110X12785889550064.
[7] Peng H, Chen C, Zhang H, Ran X. Recent development of improved clinching process. Int J Adv Manuf Technol 2020;110:3169–99. https://doi.org/10.1007/s00170-020-05978-4.
[8] Gao P, Zhang Y, Mehta KP. Metallurgical and mechanical properties of Al–Cu joint by friction stir spot welding and modified friction stir clinching. Met Mater Int 2020. https://doi.org/10.1007/s12540-020-00759-w.
[9] Shanjeevi C, Kumar SS, Sathiya P. Multi-objective optimization of friction welding parameters in AISI 304L austenitic stainless steel and copper joints. Proc Inst Mech Eng Part B J Eng Manuf 2016;230:449–57. https://doi.org/10.1177/0954405414555590.
[10] Sahin M. Joining of stainless steel and copper materials with friction welding. Ind Lubr Tribol 2009;61:319–24. https://doi.org/10.1108/00368790910988435.
[11] Li Y, Chen C, Yi R, Ouyang Y. Review: special brazing and soldering. J Manuf Process 2020;60:608–35. https://doi.org/10.1016/j.jmapro.2020.10.049.
[12] Han J, Paidar M, Vignesh RV, Mehta KP, Heidarzadeh A, Ojo OO. Effect of shoulder features during friction spot extrusion welding of 2024-T3 to 6061-T6 aluminium alloys. Arch Civ Mech Eng 2020;20. https://doi.org/10.1007/s43452-020-00086-2.
[13] Kumar D, Kore SD, Nandy A. Finite element modeling of electromagnetic crimping of Cu-SS tube-to-tube joint along with simulation of destructive testing for strength prediction of the joint. J Manuf Sci Eng 2021;143:1–11. https://doi.org/10.1115/1.4048431.
[14] Chen S, Huang J, Xia J, Zhang H, Zhao X. Microstructural characteristics of a stainless steel/copper dissimilar joint made by laser welding. Metall Mater Trans A Phys Metall Mater Sci 2013;44:3690–6. https://doi.org/10.1007/s11661-013-1693-z.
[15] Poo-arporn Y, Duangnil S, Bamrungkoh D, Klangkaew P, Huasranoi C, Pruekthaisong P, et al. Gas tungsten arc welding of copper to stainless steel for ultra-high vacuum applications. J Mater Process Technol 2020;277:116490. https://doi.org/10.1016/j.jmatprotec.2019.116490.
[16] Kuryntsev SV, Morushkin AE, Gilmutdinov AK. Fiber laser welding of austenitic steel and commercially pure copper butt joint. Opt Lasers Eng 2017;90:101–9. https://doi.org/10.1016/j.optlaseng.2016.10.008.
[17] Chen C, Zhang H, Zhao S, Ren X. Effects of sheet thickness and material on the mechanical properties of flat clinched joint. Front Mech Eng 2021. https://doi.org/10.1007/s11465-020-0618-y.
[18] Zhang X, Pan T, Flood A, Chen Y, Zhang Y, Liou F. Investigation of copper/stainless steel multi-metallic materials fabricated by laser metal deposition. Mater Sci Eng A 2021:811. https://doi.org/10.1016/j.msea.2021.141071.
[19] Gu X, Cui Z, Gu X, Shao J. Wire-feeding laser welding of copper / stainless steel using. Materials (Basel) 2021;14:1–17. https://doi.org/10.3390/ma14092122.
[20] Kimura M, Kusaka M, Kaizu K, Fuji A. Effect of post-weld heat treatment on joint properties of friction welded joint between brass and low carbon steel. Sci Technol Weld Join 2010;15:590–6. https://doi.org/10.1179/136217110X12813393169615.
[21] Fu L, Du SG. Effects of external electric field on microstructure and property of friction welded joint between copper and stainless steel. J Mater Sci 2006;41:4137–42. https://doi.org/10.1007/s10853-006-6224-5.
[22] Chen C, Zhao S, Cui M, Han X, Ben N. Numerical and experimental investigations of the reshaped joints with and without a rivet. Int J Adv Manuf Technol 2017;88:2039–51. https://doi.org/10.1007/s00170-016-8889-5.
[23] Jayabharath K, Ashfaq M, Venugopal P, Achar DRG. Investigations on the continuous drive friction welding of sintered powder metallurgical (P/M) steel and wrought copper parts. Mater Sci Eng A 2007:454–5 [114–23], https://doi.org/10.1016/j.msea.2006.11.026.
[24] Kimura M, Kusuka M, Kaizu K, Fuji A. Effect of friction welding condition on joining phenomena and tensile strength of friction welded joint between pure copper and low carbon steel. J Solid Mech Mater Eng 2009;3:187–98. https://doi.org/10.1299/jmmp.3.187.
[25] Kimura M, Kasuya K, Kusaka M, Kaizu K, Fuji A. Effect of friction welding condition on joining phenomena and joint strength of friction welded joint between brass and low carbon steel. Sci Technol Weld Join 2009;14:404–12. https://doi.org/10.1179/136217108X394744.
[26] Ambroziak A. Hydrogen damage in friction welded copper joints. Mater Des 2010;31:3869–74. https://doi.org/10.1016/j.matdes.2010.02.037.
[27] Yeoh CK, Jamaludin SB, Ahmad ZA. The effect of varying process parameters on the microhardness and microstructure of Cu–steel and Al–Al2O3 friction joints. J Teknol 2004;41:85–95. https://doi.org/10.11113/jt.v41.693.

[28] Wang Y, Luo J, Wang X, Xu X. Interfacial characterization of T3 copper/35CrMnSi steel dissimilar metal joints by inertia radial friction welding. Int J Adv Manuf Technol 2013;68:1479–90. https://doi.org/10.1007/s00170-013-4936-7.
[29] Luo J, Xiang J, Liu D, Li F, Xue K. Radial friction welding interface between brass and high carbon steel. J Mater Process Technol 2012;212:385–92. https://doi.org/10.1016/j.jmatprotec.2011.10.001.
[30] Wu W, Zhu LY, Wu GF, Bin Xu H. Study on performance of inertia radial friction welding of copper-alloy to 35CrMnSi steel. Adv Mater Res 2011:291–4 [968–74], https://doi.org/10.4028/www.scientific.net/AMR.291-294.968.
[31] Sahin AZ, Yibaş BS, Ahmed M, Nickel J. Analysis of the friction welding process in relation to the welding of copper and steel bars. J Mater Process Technol 1998;82:127–36. https://doi.org/10.1016/S0924-0136(98)00032-6.
[32] Luo J, Wang X, Liu D, Li F, Xiang J. Inertia radial friction welding joint of large size H90 brass/D60 steel dissimilar metals. Mater Manuf Process 2012;27:930–5. https://doi.org/10.1080/10426914.2011.610087.
[33] Vairamani G, Kumar TS, Malarvizhi S, Balasubramanian V. Application of response surface methodology to maximize tensile strength and minimize interface hardness of friction welded dissimilar joints of austenitic stainless steel and copper alloy. Trans Nonferrous Met Soc China (English Ed) 2013;23:2250–9. https://doi.org/10.1016/S1003-6326(13)62725-9.
[34] Ochi H, Yamamoto Y, Kawai G, Suga Y. Tensile strength of friction-welded joints of copper alloys to steels. Proc Int Offshore Polar Eng Conf 2008;8:272–6.
[35] Marimuthu S, Balasubramanian KR, Kannan TTM. Mechanical and surface morphology study of Monel – copper joint by rotary friction welding. Mater Today Proc 2020. https://doi.org/10.1016/j.matpr.2020.05.401.
[36] Vyas H, Mehta KP, Badheka V, Doshi B. Pipe-to-pipe friction welding of dissimilar Al-SS joints for cryogenic applications. J Brazilian Soc Mech Sci Eng 2020:42. https://doi.org/10.1007/s40430-020-2181-1.
[37] Vyas HD, Mehta KP, Badheka V, Doshi B. Processing and evaluation of dissimilar Al-SS friction welding of pipe configuration: nondestructive inspection, properties, and microstructure. Meas J Int Meas Confed 2021;167:108305. https://doi.org/10.1016/j.measurement.2020.108305.
[38] Shanjeevi C, Satish Kumar S, Sathiya P. Evaluation of mechanical and metallurgical properties of dissimilar materials by friction welding. Procedia Eng 2013;64:1514–23. https://doi.org/10.1016/j.proeng.2013.09.233.
[39] Fukumoto S, Tsubakino H, Okita K, Aritoshi M, Tomita T. Friction welding process of 5052 aluminium alloy to 304 stainless steel. Mater Sci Technol 1999;15:1080–6. https://doi.org/10.1179/026708399101506805.
[40] Springer H, Kostka A, Payton EJ, Raabe D, Kaysser-Pyzalla A, Eggeler G. On the formation and growth of intermetallic phases during interdiffusion between low-carbon steel and aluminum alloys. Acta Mater 2011;59:1586–600. https://doi.org/10.1016/j.actamat.2010.11.023.
[41] Muhammad N. Diffusion of elemental additives during sintering. Dissertation 2012:59 (https://doi.org/urn:nbn:se:kth:diva-100702).
[42] Kimura M, Ohara K, Kusaka M, Kaizu K, Hayashida K. Effects of tensile strength on friction welding condition and weld faying surface properties of friction welded joints between pure copper and austenitic stainless steel. J Adv Join Process 2020;2:100028. https://doi.org/10.1016/j.jajp.2020.100028.
[43] Sahin M, Çil E, Misirli C. Characterization of properties in friction welded stainless steel and copper materials. J Mater Eng Perform 2013;22:840–7. https://doi.org/10.1007/s11665-012-0310-4.